Clim. Past Discuss., 7, 1973–2019, 2011
www.clim-past-discuss.net/7/1973/2011/
doi:10.5194/cpd-7-1973-2011

Climate of the Past Discussions

Tropical climate and vegetation changes during Heinrich Event 1: comparing climate model output to pollen-based vegetation reconstructions with emphasis on the region around the tropical Atlantic Ocean

D. Handiani[1,2], **A. Paul**[1,2], **and L. Dupont**[1]

[1]MARUM – Center for Marine Environmental Sciences, University of Bremen, 28359 Bremen, Germany
[2]Department of Geosciences, University of Bremen, Bremen, Germany

Received: 31 May 2011 – Accepted: 1 June 2011 – Published: 21 June 2011

Correspondence to: D. Handiani (dhandiani@marum.de)

Published by Copernicus Publications on behalf of the European Geosciences Union.

Abstract

Abrupt climate changes associated with Heinrich Event 1 (HE1) about 18 to 15 thousand years before present (ka BP) strongly affected climate and vegetation patterns not only in the Northern Hemisphere, but also in tropical regions in the South Atlantic Ocean. We used the University of Victoria (UVic) Earth System-Climate Model (ESCM) with dynamical vegetation and land surface components to simulate four scenarios of climate-vegetation interaction: the pre-industrial era (PI), the Last Glacial Maximum (LGM), and a Heinrich-like event with two different climate backgrounds (interglacial and glacial).

The HE1-like simulation with a glacial climate background produced sea surface temperature patterns and enhanced interhemispheric thermal gradients in accordance with the "bipolar seesaw" hypothesis. It allowed us to investigate the vegetation changes that result from a transition to a drier climate as predicted for northern tropical Africa due to a southward shift of the Intertropical Convergence Zone (ITCZ). We found that a cooling of the Northern Hemisphere caused a southward shift of those plant-functional types (PFTs) in Northern Tropical Africa that are indicative of an increased desertification, and a retreat of broadleaf forests in Western Africa and Northern South America.

We used the PFTs generated by the model to calculate mega-biomes to allow for a direct comparison between paleodata and palynological vegetation reconstructions. Our calculated mega-biomes for the pre-industrial period and the LGM corresponded well to the modern and LGM sites of the BIOME6000 (v.4.2) reconstruction, except that our present-day simulation predicted the dominance of grassland in Southern Europe and our LGM simulation simulated more forest cover in tropical and sub-tropical South America. The mega-biomes from the HE1 simulation with glacial background climate were in agreement with paleovegetation data from land and ocean proxies in West, Central, and Northern Tropical Africa as well as Northeast South America. However, our model did not agree well with predicted biome distributions in Eastern South America.

CPD

7, 1973–2019, 2011

1 Introduction

Heinrich events (HE) are associated with abrupt climate changes (Bond et al., 1993; Broecker, 1994) and correlated with a slowdown or collapse of the Atlantic Meridional Overturning Circulation (AMOC) and a reduced formation of North Atlantic Deep Water (NADW) (e.g., Vidal et al., 1997; Cortijo et al., 1997; McManus et al., 2004). These events are characterized by distinct layers of ice-rafted debris in ocean sediments, which stem from the melting of large icebergs in the North Atlantic Ocean that originated from the disintegrating Laurentide ice sheet (Bond et al., 1992, 1993; Broecker et al., 1992; Hemming, 2004). Consequently, these events resulted in ice-sheet thinning and rising sea level (Yokoyama et al., 2001; Chappell, 2002; Flückiger et al., 2006).

Currently, it is debated whether the iceberg discharges were the consequence or the cause of a weakened AMOC (Flückiger et al., 2006; Clark et al., 2007), although it is widely accepted that these events impacted the climate of mid- and high latitudes in the Northern Hemisphere (e.g., Schmitter et al., 2002). In addition, several studies suggest that tropical regions are also affected by HE (Arz et al., 1998; Peterson et al., 2000; Altabet et al., 2002). These climatic shifts outside the North Atlantic Ocean imply large changes in the distribution of vegetation, likely as a result of a southward shift of the tropical rainbelt, as shown in ocean and lake records from the Cariaco Basin (Hughen et al., 2004; Gonzalez et al., 2008), Northeast Brazil (Behling et al., 2000; Ledru et al., 2006), and North West Africa (Mulitza et al., 2008).

Understanding the connection between the variability of vegetation in the Atlantic tropical regions and climate change in the Northern Hemisphere can enhance our ability to predict and explain the response of global vegetation patterns to abrupt climate changes. In the past, research has focused on processes in the Northern Hemisphere with relative success in attributing abrupt climate changes to changes in the AMOC. The tropical regions cover half of the Earth's surface, but little attention has been paid on how vegetation responds in these areas to changes in North Atlantic

CPD
7, 1973–2019, 2011

climate. Accordingly, we employ an Earth System Model of Intermediate Complexity (EMIC) (Claussen, et al., 2002) to study the effect of abrupt climate changes on tropical vegetation during HE1 (about 18 to 15 thousand years before present, ka BP). Previous studies have addressed the response time of the terrestrial biosphere to such an abrupt climate change (Scholze et al., 2003), the comparison between numerical model results and a pollen record from the Alboran Sea (Kageyama et al., 2005), the effect on global terrestrial carbon storage (Köhler et al., 2005) and the CO_2 response to AMOC changes and its contribution to the terrestrial and marine carbon cycle (Menviel et al., 2008). These models simulate HE1 by perturbing the freshwater budget of the Northern North Atlantic Ocean, given an interglacial or glacial background climate. Scholze et al. (2003) and Köhler et al. (2005) suggest an increase in carbon storage due to a southward shift in the tree line around 40° N, a replacement of tropical forests by grasslands due to drier conditions within approximately 5° S to 15° N, and wetter conditions between 10° S and 20° S. Menviel et al. (2008) find a change towards a drier climate in Equatorial and Northern South America. However, we still lack an understanding of how HE1 affected vegetation patterns in the Atlantic tropical region.

Tropical vegetation is mainly sensitive to changes in regional precipitation, which are related to shifts of the Intertropical Convergence Zone (ITCZ). The position of the ITCZ in the Atlantic tropical regions in turn is linked to the climate of the North Atlantic Ocean over the last glacial period and the Holocene, as suggested by several proxy studies (e.g., Peterson et al., 2000; Mulitza et al., 2008). During HE1, the ITCZ likely shifted southward, leading to a drier climate as indicated by a reduction in forest cover in tropical Africa and South America (e.g., Hughen et al., 2004; Menviel et al., 2008). We note, however, that according to a recent study based on a compilation of marine sediment cores from offshore tropical Western Africa the ITCZ may not shift to the south or north, but the tropical rainbelt may contract or expand symmetrically in both hemispheres in response to changes in Northern Hemisphere high-latitude climate (Collins et al., 2011). Furthermore, changes in Northern Hemisphere climate not only affected the tropics, but apparently also influenced climate in the Southern Hemisphere. This is

CPD
7, 1973–2019, 2011

expressed in the bipolar seesaw hypothesis, whereby a cooling in the Northern Hemisphere is associated with a warming in the Southern Hemisphere (Broecker et al., 1985). Records from the Southern Hemisphere indicate a higher SST during HE1 (Lamy et al., 2007; Barker et al., 2009), while several modeling studies confirm the importance of this mechanism for regional climate changes during the glacial period (Meissner et al., 2003; Crucifix et al., 2005; Roche et al., 2007). Nevertheless, how cooling in the North Atlantic Ocean and warming in the South Atlantic Ocean during HE1 are linked to changes the vegetation around the tropical Atlantic has not been clarified yet.

In our study, we examined how vegetation in the Atlantic tropical region may have responded to changes in climate and AMOC intensity during HE1. To this end, we used an EMIC containing a Dynamic Global Vegetation Model (DGVM), i.e., the University of Victoria Earth System-Climate Model (UVic ESCM, version 2.8, cf. Weaver et al., 2001). We considered the effect of a slow-down of the AMOC for two different background climate states, corresponding to the pre-industrial and the Last Glacial Maximum (LGM, about 23 to 19 ka BP) time periods. To simplify the comparison between the model results and paleovegetation reconstructions, we computed the biome distribution from the simulated plant-functional type (PFT) coverage and climate. We compare the vegetation response in the tropical Atlantic region during HE1 to other Atlantic regions and discuss the influence of the background climate state.

The paper is arranged accordingly. The model and biome analysis method is described in Sect. 2 together with the experimental setup. In Sects. 3 and 4, we present the results of the simulations for the pre-industrial, LGM and HE1 time periods in terms of the change in climate and biome distribution in the tropical Atlantic region, and we compare them to paleoclimate proxies and paleovegetation records. Section 5 discusses the results, also in comparison to other Atlantic regions and in relation to the climate state background, and the summary and conclusions appear in Sect. 6.

CPD
7, 1973–2019, 2011

2 Methods and experimental design

2.1 The UVic ESCM and TRIFFID DGVM

The UVic ESCM incorporates an energy-moisture balance atmospheric model (Fanning and Weaver, 1996), a dynamic global vegetation model (Cox, 2001), a three-dimensional ocean general circulation model (Pacanowski, 1995), and a dynamic-thermodynamic sea ice model (Hibler, 1979; Hunke and Dukowicz, 1997; Bitz et al., 2001). The model has a grid cell resolution of 3.6° × 1.8° (longitude × latitude) with one vertically-averaged layer in the atmospheric model, and 19 vertical levels in the ocean model. The annual cycle of incoming solar radiation (insolation) for present and past orbital configurations is included as an external forcing factor (Berger, 1978). In addition, we use a mean-monthly wind stress climatology, created from daily reanalysis data from 1958–1998 (Kalnay et al., 1996), to force the ocean and sea-ice components of the model.

The UVic ESCM also contains a land surface scheme MOSES 2 (Cox et al., 1999) and a DGVM called TRIFFID (Top-down Representation of Interactive Foliage and Flora Including Dynamics – Cox, 2001) as described by Meissner et al. (2003). The TRIFFID model calculates the plant distribution based on the CO_2 fluxes between land and atmosphere and as represented by the structure and coverage of five Plant Functional Types (PFTs) and soil carbon storage. The CO_2 flux depends on climate and the CO_2 concentration gradient between the land and atmosphere, which is calculated in MOSES 2. Any change in the CO_2 flux causes corresponding changes in PFT coverage and structure. In TRIFFID, carbon fluxes in each PFT are derived from the photosynthesis-stomatal conductance model developed by Cox et al. (1999), which utilizes an existing model of leaf-level photosynthesis in C_3 and C_4 plants (Collatz et al., 1991). In TRIFFID and MOSES 2, five PFTs (broadleaf trees, needleleaf trees, C_3 grasses, C_4 grasses, and shrubs) serve as vegetated land cover types. Non-vegetated land cover types consist of bare soil, inland water, and continental ice (Cox, 2001). To simplify the comparison of the TRIFFID output with available paleovegetation

CPD
7, 1973–2019, 2011

reconstructions, we developed an algorithm to compute biomes from a combination of PFTs and climate model output. For a full description, see the biome analysis Sect. 2.3.

2.2 Simulation design and boundary conditions

The control simulation (PI_CNTRL) was forced by boundary conditions characteristic of the pre-industrial period with an atmospheric CO_2 concentration of 280 ppm, a solar constant of 1365 $W\,m^{-2}$, a present-day wind field, orbital parameters from 1950 AD, and ice sheet topography and vegetation distribution from modern observations (Meissner et al., 2003), and it was integrated over a period of 2000 years to reach an (quasi-) equilibrium state. The equilibrium LGM run used the orbital parameters for 21 ka BP, an atmospheric CO_2 concentration of 200 ppm and the ICE-5G ice-sheet reconstructions for the last glacial maximum (Peltier, 1994); it was integrated over the same period of time.

To investigate Heinrich like-climate (HE1) conditions and analyze the vegetation distribution in the tropics, we forced the UVic ESCM by adding freshwater in the North Atlantic Ocean using last glacial maximum (or glacial, HE1_GL) and pre-industrial (or interglacial, HE1_IGL) boundary conditions. The two HE1 experiments started from an equilibrium state (i.e., the HE1_GL from the LGM equilibrium simulation, and HE1_IGL from the PI_CNTRL simulation). In each HE1 simulation, we added freshwater to the North Atlantic region at the St. Lawrence River mouth (Fig. 1 region A) during a 500-year period at a constant rate of 0.1 Sv (1 Sv = 10^6 $m^3\,s^{-1}$) (cf. Hemming, 2004). These two HE1 simulations with two different climate backgrounds were used to reveal differences in vegetation response with respect to a reduced and a collapsed AMOC. An overview of all simulations in this paper is given in Table 1. For all analyses, we used the mean-annual results for analyzing the climate conditions and the vegetation distribution.

CPD
7, 1973–2019, 2011

2.3 Biome analysis from TRIFFID

In order to compare the model output with paleovegetation reconstructions, we generated vegetation distributions in terms of biomes using the PFT coverage and temperatures from the UVic ESCM output. The simulated atmospheric temperature was used to calculate the parameters constraining biomes such as temperature of the coldest month (Tc), temperature of the warmest month (Tw), and the number of growing degree-days above 0 and 5 °C (GDD0 and GDD5, respectively). These constraints were chosen based on the definition of biomes in the BIOME4 model (Kaplan et al., 2003).

To attain the biome distribution, we calculated the potential PFT coverage for each grid cell based on the fractional PFT coverage (Table 2; Crucifix et al., 2005), and then combined both the environmental limitation and the potential PFTs (Table 3; Prentice et al., 1992; Harrison and Prentice, 2003; Roche et al., 2007). By a "potential PFT" we mean either the dominant PFT or a mixture of PFTs in each grid cell, which we calculated based on the percentage of PFT coverage (Table 3; Prentice et al., 1992; Harrison and Prentice, 2003; Roche et al., 2007). We finally compared the biome distribution based on the model output with biome distributions derived from paleovegetation reconstructions. To simplify the comparison, we used nine biomes which are classified as the "mega-biomes" in BIOME6000 (Harrison and Prentice, 2003), and the global data sets from Prentice et al. (2000), Harrison et al. (2001), Bigelow et al. (2003), and Pickett et al. (2004) (see also http://www.bridge.bris.ac.uk/resources/Databases/BIOMES_data). The nine biomes included are tropical forest, warm-temperate or mixed forest, temperate-montane forest, boreal forest, savanna and dry woodland, grassland and dry shrub land, desert, dry tundra, and tundra.

CPD
7, 1973–2019, 2011

3 The equilibrium simulations

Our equilibrium simulations PI_CNTRL and LGM represent two background climate states of the Earth system corresponding to pre-industrial and LGM boundary conditions. Generally the UVic ESCM reaches a near-equilibrium state after about 2000 years of integration; by that time the annually-averaged surface fluxes are close to zero (Weaver et al., 2001).

3.1 Pre-industrial simulation (PI_CNTRL)

The equilibrium climate conditions resulting from the pre-industrial control simulation (PI_CNTRL) are summarized in Fig. 2. The simulated SSTs (Fig.2b) are in general agreement with the World Ocean Atlas (Conkright et al., 1998). However, there is a cold bias in the tropical Atlantic Ocean, a warm bias along the mid-latitude Atlantic coasts (e.g. the west coast of South Africa and east coast of North America), and a cold bias in the Gulf of Alaska and the Greenland, Iceland and Norwegian seas (cf. Weaver et al., 2001). Tropical (between 30° N to 30° S) annual mean precipitation simulated in PI_CNTRL ranged from 0.1 to 2.5 m yr^{-1} (Fig. 2c). Low precipitation values (below 0.5 m yr^{-1}) occurred in Southern Africa and South America, in the high latitudes in both hemispheres, and in Northern Sub-Tropical Africa. High terrestrial precipitation (above 1.5 m yr^{-1}) occurred in Northern South America, Central North America and Central Africa, while oceanic precipitation was highest (above 2.0 m yr^{-1}) in the Eastern Pacific and Indian Oceans. Although the simulated precipitation patterns are similar to the NCEP/NCAR reanalysis data (Kalnay et al., 1996; Weaver et al., 2001) (e.g., both data and model have high precipitation in Northern South America and Central Africa), there are differences in position or intensity. For example, the simulated precipitation in Northern South America is less intense than observed. The maximum of precipitation was simulated in the Western Pacific Ocean, while the data shows it in North-Western South America.

CPD
7, 1973–2019, 2011

The evaporative loss over the oceans simulated in PI_CNTRL reached approximately 1.5 to 2.0 m yr^{-1}, and in some cases more than 2.0 m yr^{-1} (Fig. 2d). Evaporation in northern and southern high latitudes, as well as in subtropical regions such as Northern Africa, the Middle East, and Australia, was relatively low (below 0.4 m yr^{-1}). In Northern South America and Central Africa, the evaporative loss from land was estimated as about 1.0 m yr^{-1}, which was less than over the neighbouring North or South Atlantic Oceans. These patterns in the PI_CNTRL simulation correspond well to the NCEP/NCAR data, which also shows low evaporation rates in Northern Africa and Australia and high evaporation rates in Northern South America and Central Africa. Our simulation compares better to observations than the present-day simulation by Weaver et al. (2001), possibly because our version of the UVic ESCM includes a DGVM that leads to a more realistic representation of the hydrological cycle.

The PI_CNTRL simulation also indicated a net gain of freshwater in Northeast and Southern South America, as well as in Central Africa (Fig. 2e). A net gain of freshwater corresponds to more precipitation than evaporation, leading to better conditions for a more robust tree cover (e.g. tropical forest).

The zonally integrated meridional overturning circulation in the Atlantic Ocean (AMOC) for the PI_CNTRL simulation indicates a North Atlantic Deep Water (NADW) cell and an Antarctic Bottom Water (AABW) cell (Fig. 2f). This pattern is typical of an active mode of the Atlantic thermohaline circulation under conditions similar to the present day. The maximum of the streamfunction was 21 Sv and found between 35° and 40° N at 1000 m depth. The export of NADW across the equator into the South Atlantic Ocean was about 14 Sv, which is comparable to observations (for example, Lumpkin and Speer, 2007, give a value of 17.9 ± 3.1 Sv). The AABW that originated from the Southern Ocean flowed across the equator into North Atlantic Ocean at a rate of 2 Sv and penetrated as far north as about 20° N.

The vegetation cover in the UVic ESCM is represented by PFTs, which in our study were used to calculate the biome distribution. Figure 3 shows the annual-mean PFT distribution for the PI_CNTRL simulation as a fraction of the area covered in each grid

CPD
7, 1973–2019, 2011

cell of the model. Broadleaf trees were dominant in the tropics (e.g. in South America, Africa, and the Indo-Pacific region between 15° N to 15° S). Needleleaf trees were dominant in northern high latitudes such as Northern Siberia and North America, but also at high elevation in Northern India (Himalayan Mountains), where the fractional cover is between 40 to 90 %. The C_3 grasses covered a large area of the globe and reached high percentages in Northern Eurasia and North America. The C_4 grasses were simulated in Southeast Africa with low percentages (around 10 %), while a coverage of more than 80 % was reached in North Africa, Northern India, and Australia. This type of grasses is better adapted to a moist and hot climate, while the C_3 grasses grow preferentially in a cooler and wetter climate. Shrubs are also representative of a cooler climate and occur together with needleleaf trees in Northern Siberia and North America. Our results mostly agree with the PFT distribution simulated by Meissner et al. (2003), except that they obtain more broadleaf trees in Central America and a higher percentage (mostly above 60 %) of needleleaf trees in the northern high latitudes.

The biome distribution is plotted in Fig. 4. A high fractional coverage of tropical forest is shown in Northern South America in areas such as the Amazon rain forest, Northern Brazil, Venezuela, Colombia, and Peru. The tropical forest cover, represented by the broadleaf trees PFT in the model, was similar to results by Meissner et al. (2003) and Crucifix et al. (2005). However, our model simulated tropical forest in Northern Venezuela and Northeast Brazil, whereas according to reconstructions by Loveland et al. (2000) and the BIOME4 model (Kaplan et al., 2003; Fig. 4b) these regions are covered by savannah, grassland, and shrubland.

In our control simulation, tropical North America was dominated by tropical forest, although we find small areas of savannah in Central America. This biome pattern agrees with Kaplan et al. (2003), who obtain tropical forest, savannah, and temperate forest in this region, and it is also similar to the findings by Crucifix et al. (2005) and Meissner et al. (2003), who predict a dominance of tropical forest biomes over broadleaf forest cover. Sub-tropical North America was estimated to be dominated mostly by grassland while small areas of boreal and temperate forests were found in Central North

CPD
7, 1973–2019, 2011

America. However, a different distribution is reported by Crucifix et al. (2005), Meissner et al. (2003) and Kaplan et al. (2003) who estimate a dominance of temperate and boreal forest, and also regionally of desert and grassland. Observations by Loveland et al. (2000) and the BIOME 6000 project (Fig. 4c) conclude that the area is dominated by open shrubland or savannah in Western North America, grasslands in the central region, and mixed boreal and temperate forest in Eastern North America. Thus our model did not reproduce the observed vegetation distribution in North America, neither regarding location nor in terms of the general pattern. The discrepancy is likely due to an overestimation of C_3 grasses precluding the simulation of dominant tree cover and hence, the formation of mixed boreal and temperate forest mega-biomes.

In experiment PI_CNTRL, we simulated tropical forests in Western and Central Africa between 20° N and 20° S. In the Sahel region and along the east coast of Africa, the biome distribution was mostly savannah, while to the south it was mixed grassland and warm temperate forest prevailed. These patterns generally agree with both the BIOME4 model and BIOME 6000 data (Fig. 4b, c). The BIOME 4 model estimates grassland and savannah in the Sahel, tropical forest along the west coast and extending into the Central Africa (Angola, Congo, and Zambia), and grasslands in Eastern Africa. The BIOME 6000 data shows mostly tropical forest in Western Equatorial Africa, and grassland and savannah in the Sahel. Our model failed to simulate desert and savannah at the southern tip of Africa, where the BIOME4 model and BIOME 6000 data show a mix of savannah, desert, warm-temperate forest, and grassland. Another discrepancy occurs in Southern Europe, where the biomes estimated in the PI_CNTRL simulation did not reveal a warm-temperate forest as evidenced by data from the BIOME 6000 project. It seems that our model overestimated the growth of C_3 grasses in those areas, and hence Europe and Eurasia were covered by the grassland biome.

CPD
7, 1973–2019, 2011

3.2 Last Glacial Maximum simulation (LGM)

The LGM simulated SAT and SST cooler than PI_CNTRL (Fig. 5a, b), largest SAT cooling occurred near the ice sheets (up to −20 °C and −40 °C different from PI_CNTRL in North America and in Antarctic, respectively). However, there was also a moderate cooling of SAT in the tropics (Fig. 5a) where differences between LGM and PI_CNTRL were around 3 °C. The largest SST anomaly occurred in the Western North Atlantic Ocean where the differences between LGM and PI_CNTRL reached more than 9 °C, while the cooling in the tropics amounted to 3 and 2 °C (Fig. 5b). The LGM precipitation patterns are overall similar to our PI_CNTRL, except that the intensity was reduced by 0.3 to 0.5 m yr^{-1} (Fig. 5c).

As in the PI_CNTRL simulation, the AMOC in the LGM simulation (Fig. 5d) was also in the active mode. The maximum of the meridional overturning streamfunction was 7 Sv less than in the PI_CNTRL simulation (13.5 Sv as compared to 21 Sv), located further south and at a slightly shallower depth (~ 100 m less). NADW was transported across the equator and exported to the South Atlantic Ocean at a rate reduced by about 40 % (from 14 Sv to 8 Sv), while the inflow of AABW from the South Atlantic Ocean was similar (2 Sv) but reached further northward (up to 25° N) to replace part of the NADW.

Differences between the LGM simulation and the PI_CNTRL simulation were most pronounced in Northern and Eastern Africa and Western South America (Fig. 6a), where drier biomes were predicted for the LGM. Otherwise, our LGM results were similar to those of our PI_CNTRL simulation (Figs. 4a and 6a), especially in Northern Tropical South America (tropical forest) and Southern South America (grassland and dry-shrubland) although we found a few locations in South America where the biome distribution was different. In Western South America, warm-temperate forest changed to boreal forest, and warm-temperate forest extended from Middle and Eastern Brazil to Western Brazil, indicating reduced temperature and precipitation that affected the PFT coverage in the LGM simulation. The LGM simulation also indicated drier conditions in Southeast South America by the presence of grasslands and shrublands. Our results

CPD
7, 1973–2019, 2011

generally agree with the LGM simulation by Crucifix et al. (2005) and Henrot et al. (2009), which shows a dominance of open vegetation and C_3 grasses. Paleovegetation reconstructions from plant fossil and proxy data sources such as in Ray and Adams (2001) also suggest drier conditions in these areas which are dominated by desert and semi-desert.

In Central North America temperate forest was partly replaced by boreal forest. The vegetation in our LGM simulation showed a similar bias in North America as the PI_CNTRL simulation. The C_3 grass cover was overestimated in comparison to other simulations (e.g., Crucifix et al., 2005; Roche et al., 2007), which predict a dominance of cool forest biomes such as needleleaf, mixed and temperate broadleaf forests, even though they also simulate warm grasses and savannah in eastern regions and tropical forest in western regions. Similarly, the BIOME 6000 project reconstructions predict boreal and temperate forest in Eastern North America but a dominance of savannah in Western North America. All models seem to be consistent with the proxy data that indicate the presence of a more humid vegetation during the LGM compared to present day, although the location and biome type do not exactly match those from proxy estimations.

Our LGM simulation yielded warm-temperate forest and grassland in the Sahel region in contrast to tropical forest and savannah in the PI_CNTRL simulation. The LGM tropical forest cover showed a similar pattern but with a lower percentage than in the PI_CNTRL simulation. A decrease in tropical forest in Central Africa is consistent with a lower temperature and reduced precipitation during the LGM (Figs. 2 and 5). This pattern agrees with reconstructions by Ray and Adams (2001) and Dupont et al. (2000), who found a reduction in tropical forest in Western and Central Africa during the LGM period. Our model also agrees with pollen data from BIOME 6000 which show tropical forest on the west coast of Africa and grasslands in Southern Africa, desert cover in Northern Africa, and a vegetation change from savannah to grassland, and tropical forest to warm-temperate forest in Central Africa.

CPD
7, 1973–2019, 2011

Both equilibrium climate simulations PI_CNTRL and LGM predicted similar dominant biomes in the Indonesian Archipelago (tropical forest) and in Australia (savannah, grassland, and desert). The difference in biomes between the pre-industrial and LGM simulations is only through a reduction in vegetation cover, where savannah in Northern Australia and grasslands in Southern Australia were replaced by desert. Our results for Southern Australia were consistent with the LGM simulation by Roche et al. (2007) and supported by proxy data (Harrison and Prentice, 2003).

4 Heinrich Events 1 simulations

4.1 Changes in climate

Our HE1 simulations corresponded to a $1.6 \times 10^6\,km^3$ release of freshwater and an associated global sea level rise of 4.5 m after 500 years. This amount of water was enough to cause cessation of NADW formation in the HE1_GL simulation, while in the HE1_IGL simulation it was only reduced from 21 Sv to 16 Sv (Fig. 7). Correspondingly, the surface salinity in the North Atlantic Ocean was strongly reduced by up to 5 psu in the HE1_GL simulation (in particular near the St. Lawrence River mouth and off Western Europe and Northwest Africa), while the surface salinity in the HE1_IGL simulation was only reduced by 0.5 psu. In the South Atlantic Ocean, the strongest SSS anomaly of up to 1 psu occurred off Southwest Africa (Fig. 8, left side). These findings are consistent with other studies examining changes in AMOC strength after adding freshwater to the Northern Hemisphere to imitate the HE1 period and showing either a decrease in the AMOC strength (Weaver et al., 2003) or a complete collapse (Menviel et al., 2008; Köhler et al., 2005) followed by a cooling in the North Atlantic Ocean during HE1.

The HE1 simulations were characterized by cooling over the Northern North Atlantic Ocean (Fig. 8, middle side). This cooling was most pronounced in the HE1_GL simulation with SAT anomalies below −2.7 °C, (Fig. 8, top middle) while in the HE1_IGL

CPD
7, 1973–2019, 2011

simulation the largest negative anomaly was only around −0.5 °C (Fig. 8, bottom middle). Our HE1_GL anomaly is consistent with Menviel et al. (2008) and Kageyama et al. (2010), who also found a stronger North Atlantic cooling in their HE1 simulation using a glacial climate state as a background. Furthermore, slightly warmer SATs were found in the Southern Hemisphere and the North Pacific region, with maximum positive anomalies in the HE1_GL simulation exceeding 0.6 °C. The largest positive anomalies in the HE1_IGL simulation were only around 0.3 °C, and occurred over the tropical Indo-Pacific Ocean (Southern India, Northern Australia, and Southeast Asia).

The SST anomalies of the HE1 simulations reflect the bipolar seesaw effect in the North and South Atlantic Oceans (Fig. 8, right side), which in turn is connected to precipitation changes in the tropics. The largest negative SST anomaly occurred in the Eastern North Atlantic Ocean and reached around −4 °C in the HE1_GL simulation (Fig. 8, top right). The largest positive SST anomaly (above 1.8 °C) appeared along the southwest coast of Southern Africa and at the high latitudes of the South Atlantic Ocean.

The precipitation response was strong in the HE1_GL simulation (Fig. 9, top left), while it was negligible in the HE1_IGL simulation (Fig. 9, bottom left). Precipitation decreased in the Sahel region, the Middle East, Europe and around the Gulf of Mexico, with maximum negative precipitation anomalies of $-0.2\,\mathrm{m\,yr^{-1}}$. Precipitation increased in Southwest Africa (Angola and Namibia) and Southeast Argentina, with maximum positive anomalies exceeding $0.16\,\mathrm{m\,yr^{-1}}$. In contrast, in the HE1_IGL simulation estimated anomalies were between $-0.02\,\mathrm{m\,yr^{-1}}$ and $+0.02\,\mathrm{m\,yr^{-1}}$, only. A similar anomaly pattern is also found in other studies (e.g., Köhler et al., 2005; Menviel et al., 2008; Kageyama et al., 2010), in which it is attributed to a southward shift of the ITCZ.

The net surface freshwater flux (precipitation minus evaporation minus runoff) anomaly between the HE1_GL and the LGM simulations over the Atlantic Ocean suggests that most of the North Atlantic Ocean gained more freshwater than it received. The opposite pattern is found in the Northern and Southern Subtropical Atlantic Ocean, while the net surface freshwater flux remained nearly the same in the tropical Atlantic

CPD
7, 1973–2019, 2011

Ocean (Fig. 9, top right). The net surface freshwater flux anomaly under pre-industrial boundary conditions (Fig. 9, bottom right) had a pattern similar to that with LGM boundary conditions, except that the intensity was reduced due to the different response to the freshwater perturbation in these two climate states.

The slowdown of the AMOC and reduced deepwater formation in the HE1 simulations (Fig. 7) were associated with a seesaw pattern in temperature and precipitation at the sea surface (Figs. 8 and 9). The freshwater discharges to the North Atlantic Ocean changed the density of surface water, prevented the NADW from sinking and resulted in a reduction or shutdown of deep water formation. The AMOC stream function for the HE1_GL simulation (Fig. 7a) shows that the formation of NADW collapsed and AAIW (Antarctic Intermediate Water) became the dominant water mass, spreading further north until 20° N. The AMOC stream function in the HE1_IGL simulation (Fig. 7b) is similar to that of the PI_CNTRL simulation (Fig. 2f), except that the maximum strength was reduced from 21 Sv to 16 Sv. The weak AMOC response in HE1_IGL corresponds to weak changes in SST and precipitation.

4.2 Changes in vegetation

The HE1_GL simulation showed a much more pronounced vegetation change than the HE1_IGL simulation (Fig. 10). This is most evident in Northern North Africa (Sahel region) and Western Asia (near present-day East Kazakhstan). These changes corresponded to changes in climate, as for example in the Sahel region, where precipitation was reduced by 0.2 m yr^{-1} in the HE1_GL simulation as compared to the LGM equilibrium simulation (Fig. 9, top left). This resulted in a change in PFT coverage from robust broadleaf and needleleaf forest to grassland and shrubland cover (tree cover was reduced by more than 60 %). In other parts of the Sahel, grass and shrub covers decreased by more than 60 % and were replaced by desert. These vegetation changes, from forest to grass and shrubs, and from grass and shrubs to desert, indicate a drier climate in the HE1 simulation than in the LGM equilibrium simulations.

CPD
7, 1973–2019, 2011

South of the equator, the vegetation response in the HE1_GL simulation corresponding to a slight warming was not as robust as north of the equator. For example, in Southwest Africa precipitation increased regionally, consequently broadleaf trees cover increased by 49 %, while at the same time grass and shrub cover decreased by 51 % (Fig. 10). In the HE1_IGL simulation, changes were much smaller or even insignificant (increase or decrease are less than 10 %). Grass and shrub cover in northern tropical and sub-tropical regions (0 to 30° N) in the HE1_GL simulation went almost unchanged, except for a small region at the edge of West Africa, where grasses increased by around 20 % and consequently trees decreased by a similar amount. Both HE1 simulations indicated cooler and drier climatic conditions around the North Atlantic Ocean and a succession in vegetation cover in Northern Africa from forest to grassland and from shrub to desert. Over the South Atlantic region, the HE1 simulations resulted in warmer and wetter climatic conditions in parallel with a regional increase of tropical forest cover in Southwest Africa. However, the increase in precipitation in South America in the HE1 simulations did not cause a change in vegetation cover compared to the equilibrium simulations. The vegetation response in Southwest Africa generally agrees with Menviel et al. (2008) who found that a wetter climate in the Southern Hemisphere did not lead to large changes in land carbon storage, and resulted in less forest cover in the Southern Hemisphere except for Southwest Africa and Western South America.

4.3 Biome distribution and model-data comparison

To compare the HE1 simulations with vegetation proxies, we focus on the discussion of vegetation changes in the HE1_GL simulation. The biome distribution diagnosed from our HE1_GL simulation agrees with pollen records from Equatorial Africa and South America (Fig. 11 and Table 4, Hessler et al., 2010). Both the climate and the biome distribution exhibited a shift towards drier conditions in tropical Africa, while wetter conditions existed in South America and South Africa. The tropical African biomes (not including the Sahel) were dominated by tropical forest from west to Central Africa (e.g., Gabon, Congo, Cameroon, Nigeria, Zaire, and Burundi), while in the east (e.g.,

CPD
7, 1973–2019, 2011

Tanzania and Kenya) a mix of warm temperate, boreal forest, and savannah was simulated (Fig. 11), in accordance with a wetter climate. Even when the differences in climate were not pronounced, e.g. between West and East Africa, distinctly different biomes were established. The simulated tropical African vegetation generally agrees with several palynological vegetation reconstructions in West and East Africa (Hessler et al., 2010; Kageyama et al., 2005). However, in Burundi (Central Africa), proxy records indicate a cool and dry climate dominated by grassland and savannah, while our model predicted tropical forest (Table 4). Furthermore, these records indicate that Northern Tropical Africa (i.e. the Sahel region) experienced drier conditions suggesting that the biomes changed from grasslands to desert in Eastern Sahel, warm-temperate forest to grasslands in Western Sahel, and tropical forest to warm-temperate forest in Central Sahel. This supports our model result in that due to changes in climate the PFT cover in the Sahel region changed from forests to grasses or from shrubs to desert.

The changes in biome distribution from the HE1_GL simulation in Northern and Southern Subtropical Africa show opposing trends towards drier biomes in the north and wetter biomes in the south, but the changes south of the equator are far smaller than those north of it. In Northern Subtropical and Equatorial Africa, our model suggested a drier climate, accordingly desert cover expanded in these regions. Furthermore, our model suggested the dominance of grassland in Southern Europe, which agrees with pollen reconstructions from the Mediterranean (Kageyama et al., 2005) that suggest an increase in grasslands due to a lower coldest-month temperature.

The HE1_GL simulation did not indicate major biome changes in tropical South America as compared to the LGM simulation (Fig. 11). In Northeast Brazil, the model simulated tropical forest instead of steppe and semi-desert as suggested by pollen reconstructions (Hessler et al., 2010) although the precipitation and surface air temperature decreased from LGM to HE1 (Figs. 9, top left and 8, top middle). Northern tropical South America (e.g., Venezuela) climate was drier with a maximum precipitation anomaly of around $-0.08\,\mathrm{m\,yr^{-1}}$ (Fig. 9, top left). However the tropical forest remained (Fig. 11), although biogeochemical data from this region suggest an increase

CPD
7, 1973–2019, 2011

in savannah cover (Jennerjahn et al., 2004), and palynological data of older Heinrich events (HE3, HE4, HE5, HE5a and HE6) also indicate an increase in savannah (Hessler et al., 2010). Northwest South America received less precipitation in the HE1_GL simulation. Again, the biome distribution remained similar to the LGM simulations, while reconstructions from La Laguna de Bogotá in Colombia indicate savannah and grassland (Hessler et al., 2010). Discrepancies in Northern South America indicate that climate changes of the HE1_GL simulation were not strong enough to influence the biome coverage, or that our vegetation model was not sensitive enough. On the other hand, our biome distribution in Northwest Brazil of the HE1_GL simulation is in good agreement with reconstructions from Lake Caçó (Hessler et al., 2010), where tropical forests are dominant and indicate a wetter climate during HE1 period. Furthermore, the HE1_GL simulation also predicted a dominance of desert in the Middle East and Western Asia and Arabia, while tundra expands in Northern Eurasia, in Siberia, and over the Tibetan Plateau.

5 Discussions

Our two equilibrium simulations represent warm and cold conditions during interglacial and glacial climates and provide two different backgrounds for the HE1 simulations. The largest cooling in air and sea-surface temperature between the PI_CNTRL and LGM simulations in the North Atlantic Ocean was due to the presence of ice-sheets in North America. However, the most recent SST reconstruction by the MARGO project (2009) shows a more pronounced cooling in the Eastern North Atlantic Ocean than in the Western North Atlantic Ocean. The disagreement with our model results is most likely due to misplaced deepwater formation sites in the pre-industrial control experiment. It also occurs in other coupled atmospheric-ocean models that simulate the LGM climate with a cold anomaly in the North Atlantic Ocean with a different location or magnitude (Kageyama et al., 2006).

CPD
7, 1973–2019, 2011

In the tropics, the SAT difference between the PI_CNTRL and LGM simulation is ~ 1 °C over land and ~ 2 °C over the Atlantic Ocean, while the SST differences is 2–3 °C, in agreement with the MARGO reconstruction (MARGO, 2009) and other modeling studies (e.g., Crucifix et al., 2005; Otto-Bliesner et al., 2006; Kageyama et al., 2006; Roche et al., 2007). The general agreement with reconstructions from proxy data made the LGM simulation a suitable background climate for our Heinrich event 1 simulation.

The warm (PI_CNTRL) and cold (LGM) background climate states also differed in the AMOC, with a reduced formation of NADW and a stronger AABW inflow into the Atlantic Ocean in the LGM state. This is in agreement with some other model simulations (e.g., Weaver et al., 2001; Weber and Drijfhout, 2007; Kageyama et al., 2010), but at odds with others (e.g., Roche et al., 2007; cf. Otto-Bliesner et al., 2007). However, proxy data (Pa/Th ratios) from ocean sediment cores suggest a weaker AMOC strength during the LGM period (Yu et al., 1996; Marchal et al., 2000; McManus et al., 2004; Gherardi et al., 2005), although they are difficult to interpret (e.g., Roche et al., 2007). McManus et al. (2004) analyze a high accumulation core from the deep Western Subtropical Atlantic at a depth of 4.5 km, and according to their results, the AMOC during the LGM was reduced by 30 % as compared to the present day, in broad agreement with our LGM simulation (Figs. 2f and 5d).

The two different climatic background conditions corresponding to two different states of the AMOC did not change the predicted vegetation distribution (Figs. 4, 5a, and 6a) except in a few locations: in North and Central Africa (the Sahel region), Western South America, and Central North America. For example, in North and Central Africa, a warmer and wetter climate was predicted in the PI_CNTRL simulation as compared to the LGM simulation. This resulted in more tropical forest and savannah in the PI_CNTRL simulation, while warm-temperate forest and grassland cover were extended in the LGM simulation. In general, most changes in the vegetation encompass rather small areas. We may suspect that the initial vegetation conditions for the vegetation model or the relative simplicity of the land-atmosphere model caused the similar vegetation cover estimates of the PI_CNTRL and LGM simulations. However, Hughen

CPD
7, 1973–2019, 2011

et al. (2004) show that the TRIFFID DGVM is insensitive to the choice of the initial vegetation cover, and Meissner et al. (2003) show that coupling the TRIFFID model to the UVic ESCM results in predicted vegetation patterns that compare reasonably well to observations.

Areas that were sensitive to changes in vegetation cover in the equilibrium simulations (e.g., Northern Africa, Southwest Africa and South America) also showed vegetation changes in the HE1 simulations. The key climate parameters which influence vegetation cover are temperature and precipitation. Our model results from the Heinrich event 1 simulations showed that these climate factors respond to changes in NADW formation. The AMOC reduction or collapse following the freshwater perturbation caused temperature and precipitation changes (Figs. 8 and 9), and those changes drove a subsequent response in the vegetation distribution, especially around the sub-tropical North Atlantic Ocean (Fig. 10). In the HE1_GL simulation, the AMOC collapsed (Fig. 7a) and the associated heat transfer from low to high latitudes in the Atlantic Ocean was strongly reduced. The HE1_IGL simulation indicated only a slight reduction of the AMOC strength (Fig. 7b), resulting in less pronounced climate changes and consequently less vegetation response.

6 Summary and conclusions

This study presents the distribution of vegetation simulated by the UVic Earth system-climate model including a dynamic vegetation module, for four scenarios: pre-industrial (PI_CNTRL), freshwater perturbation of the PI_CNTRL equilibrium (HE1_IGL), last glacial maximum (LGM), and freshwater perturbation of the LGM equilibrium simulating Heinrich event 1 (HE1_GL). We investigated the effects of climate change in the tropical region during Heinrich event 1 by adding freshwater to the North Atlantic. This resulted in a collapse of the Atlantic Meridional Overturning Circulation (AMOC) associated with a cooling of the Northern Hemisphere, followed by a warming of the Southern Hemisphere (the bipolar seesaw hypothesis) and a strengthening of the interhemispheric

CPD
7, 1973–2019, 2011

thermal gradient. Changes in rainfall patterns resulted in a shift of biomes in the tropical and subtropical regions.

The two equilibrium simulations (PI_CNTRL and LGM) allowed to analyze the response of the vegetation cover around the tropical Atlantic region to a freshwater perturbation in North Atlantic Ocean under different climatic background conditions. Our PI_CNTRL biomes were in general agreement with modern and Holocene biome reconstructions. Discrepancies occurred with respect to the simulation of the dominance of grasslands in Southern Europe and the failure to simulate a mixture of savannah and warm-temperate forests along the east coast of South America for the pre-industrial period. The climate and biome patterns of tropical and sub-tropical South America of our LGM simulation differ from other model results (Roche et al., 2007) and a data compilation (Ray and Adams, 2001) by suggesting wetter conditions and more forest cover.

The SSTs of the HE1 simulations exhibited the bipolar seesaw pattern that resulted from a diminished inter-hemispheric heat exchange after a slowdown or collapse of the AMOC. The model indicated a southward shift of the southern desert boundary in Northern Africa, but failed to mimic expected changes in Eastern South America. The vegetation responded similarly during the HE1 simulations under interglacial (pre-industrial) and glacial (LGM) climatic background conditions, except for Northern Tropical Africa, Western Eurasia, and Western South America. The magnitude of the changes in the tree and grass PFTs is larger for glacial than for interglacial climatic background conditions. The HE1 simulations produced a cooler climate in the Northern Hemisphere, a drier climate in Northern Tropical Africa, a local warming in Southern Hemisphere, and an apparent southward shift of the ITCZ (e.g., Menviel et al., 2008; Kageyama et al., 2009; Swingedouw et al., 2009). In addition, the vegetation responded to a changing climate through an increase in non-forested and desert PFT coverage in Northern Tropical Africa, and a change from warm-temperate to tropical forests in Southwestern Africa.

CPD
7, 1973–2019, 2011

The biome comparison between the HE1 simulations and several proxy data compilations for Equatorial and Extra-tropical Africa and South America showed reasonable agreement in vegetation patterns with both ocean records from the Mediterranean, Northwest Africa and Southwest Africa (Angola) as well as land records from Northwest Brazil (Lake Caçó) and Central Africa (Lake Tanganyika). Limitations in the number of PFTs and modeled biomes on the one hand and the lack of precision of the palynologically reconstructed biomes on the other hand, lead to differences that are difficult to assess. Improvements in the dynamic vegetation modeling can be achieved by the addition of more PFTs and specific climatic limitations to the defined plant functional types (e.g. one broadleaved forest PFT versus two, a tropical and deciduous broadleaved forest PFT). Nevertheless, the simulations showed that the collapsed AMOC heavily influenced North Atlantic climate, and this corresponded to vegetation changes in equatorial areas within HE1.

Acknowledgement. This work was funded by the Deutsche Forschungsgemeinschaft (DFG) as part of the German contribution to the Integrated Ocean Drilling Program (SPP 527) "Abrupt Climate Change in the African Tropics (ACCAT)" and DFG Research Center/Excellence Cluster "The Ocean in the Earth System".

References

Altabet, M. A., Higginson, M. J., and Murray, D. W.: The effect of millennial-scale changes in Arabian Sea denitrification on atmospheric CO_2, Nature, 415, 159–162, 2002.

Arz, H. W., Pätzold, J., and Wefer, G.: Correlated millenial-scale changes in surface hydrography and terrigenous sediment yield inferred from last-glacial marine deposits off Northeastern Brazil, Quaternary Res., 197, 323–333, 1998.

Barker, S., Diz, P., Vautravers, M. J., Pike, J., Knorr, G., Hall., I. R., and Broecker, W. S.: Interhemispheric Atlantic seesaw response during the last deglaciation, Nature, 457, 1097–1101, 2009.

Behling, H., Arz, H. W., Pätzold, J., and Wefer, G.: Late Quaternary vegetational and climate

CPD

7, 1973–2019, 2011

dynamics in Northeastern Brazil, inferences from marine core GeoB 3104-1, Quaternary Sci. Rev., 19, 981–994, 2000.
Berger, A. L.: Long-term variations of daily insolation and quaternary climate change, J. Atmos. Sci., 35, 2362–2367, 1978.
Bigelow, N. H., Brubaker, L. B., Edwards, M. E., Harrison, S. P., Prentice, I. C., Anderson, P. M., Andreev, A. A., Bartlein, P. J., Christensen, T. R., Cramer, W., Kaplan, J. O., Lozhkin, A. V., Matveyeva, N. V., Murray, D. V., McGuire, A. D., Razzhivin, V. Y., Ritchie, J. C., Smith, B., Walker, D. A., Gajewski, K., Wolf, V., Holmqvist, B. H., Igarashi, Y., Kremenetskii, K., Paus, A., Pisaric, M. F. J., and Vokova, V. S.: Climate change and Arctic ecosystems. I. Vegetation changes north of 55° N between the Last Glacial Maximum, mid-Holocene and present, J. Geophys. Res., 108(D19), 8170, doi:10.1029/2002JD002558, 2003.
Bitz, C. M., Holland, M., Weaver, A. J., and Eby, M.: Simulating the ice-thickness distribution in a coupled climate model, J. Geophys. Res., 106, 2441–2464, 2001.
Bond, G., Heinrich, H., Broecker, W., Labeyrie, L., McManus, J., Andrews, J., Huon, S., Jantschik, R., Clasen, S., Simet, C., Tedesco, K., Klas, M., Bonani, G., and Ivy, S.: Evidence for massive discharges of icebergs into the North Atlantic ocean during the last glacial period, Nature, 360, 245–499, 1992.
Bond, G. C., Broecker, W. S., Johnsen, S., McManus, J., Labeyrie, L., Jouzel, J., and Bonani, G.: Correlation between climate records from the North Atlantic sediment and Greenland ice, Nature, 365, 143–147, 1993.
Broecker, W. S.: Massive iceberg discharges as triggers for global climate change, Nature, 372, 421–424, 1994.
Broecker, W. S., Bond, G. C., Klas, M., Clark, E., and McManus, J.: Origin of the Northern Atlantic's Heinrich events, Clim. Dynam., 6, 265–273, 1992.
Broecker, W. S., Peteet, D. M., and Rind, D.: Does the ocean-atmosphere system have more than one stable mode of operation?, Nature, 315, 21–26, 1985.
Chappell, J.: Sea-level changes forced ice breakouts in the Last Glacial cycle: new results from coral terraces, Quaternary Sci. Rev., 21, 1229–1240, 2002.
Clark, P. U., Hostetler, S. W., Pisias, N. G., Schmittner, A., and Meissner, K. J.: Mechanisms for a ∼7-kyr climate and sea-level oscillation during Marine Isotope Stage 3, in: Ocean Circulation: Mechanisms and Impacts, Geophysical Monograph 173, 209–246, AGU, Washington, DC, 2007.
Claussen, M., Mysak, L. A., Weaver, A. J., Crucifix, M., Fichefet, T., Loutre, M.-F., Weber, S. L.,

CPD
7, 1973–2019, 2011

Alcamo, J., Alexeev, V. A., Berger, A., Calov, R., Ganopolski, A., Goosse, H., Lohmann, G., Lunkeit, F., Mokhov, I., Petoukhov, V., Stone, P., Wang, Z.: Earth system models of intermediate complexity: closing the gap in the spectrum of climate system models, Clim. Dynam., 18, 579–586, 2002.

Collatz, G. J., Ball, J. T., Grivet, C., and Berry, J. A.: Physiological and environmental regulation of stomatal conductance, photosynthesis and transpiration: a model that includes a laminar boundary layer, Agric. Forest Meteorol., 54, 107–136, 1991.

Collins, J. A., Schefuß, E., Heslop, D., Mulitza, S., Prange, M., Zabel, M., Tjallingi, R., Dokken, T. M., Huang, E., Mackensen, A., Schulz, M., Tian, J., Zarriess, M., and Wefer, G.: Interhemispheric symmetry of the tropical African rainbelt over the past 23 000 years, Nat. Geosci., 4, 42–45, doi:10.1038/ngeo1039, 2011.

Conkright, M. E., Levitus, S., O'Brien, T., Boyer, T. P., Stephens, C., Johnson, D., Stathoplos, L., Baranova, O., Antonov, J., Gelfeld, R., Burney, J., Rochester, J., and Forgy, C.: World Ocean Database 1998 Documentation and Quality Control, available at: http://iridl.ldeo.columbia.edu/SOURCES/.NOAA/.NODC/.WOA98/.ANNUAL/., National Oceanographic Data Center, Silver Spring, MD, 1998.

Cortijo, E., Labeyrie, L., Vidal, L., Vautravers, M., Chapman, M., Duplessy, J. C. Elliot, M., Arnold, M., Turon, J. L., and Auffret, G.: Changes in sea surface hydrology associated with Heinrich event 4 in the North Atlantic Ocean between 40° N and 60° N, Earth Planet. Sci. Lett., 146, 29–45, 1997.

Cox, P. M.: Description of the "TRIFFID" dynamic global vegetation model, Hadley Centre Technical Note 24. Met Office, Bracknell, 2001.

Cox, P. M., Betts, R. A., Bunton, C. B., Essery, R. L. H., Rowntree, P. R., and Smith, J.: The impact of new land surface physics on the GCM simulation of climate and climate sensitivity, Clim. Dynam., 15, 183–203, 1999.

Crucifix M., Betts, R. A., and Hewitt, C. D.: Pre-industrial-potential and Last Glacial Maximum global vegetation simulated with a coupled climate-biosphere model: diagnosis of bioclimatic relationships, Global Planet. Change, 45, 295–312, 2005.

Dupont, L. M., Jahns, S., Marret, F., and Ning, S.: Vegetation change in Equatorial West Africa: time-slices for the last 150 ka, Palaeogeogr. Palaeocl. 155, 95–122, 2000.

Fanning, A. G. and Weaver, A. J.: An atmospheric energy-moisture model: climatology, interpentadal climate change and coupling to an ocean general circulation model, J. Geophys. Res., 101, 15111–15128, 1996.

CPD
7, 1973–2019, 2011

Flückiger, J., Knutti, R., and White, J. W. C.: Oceanic processes as potential trigger and amplifying mechanisms for Heinrich events, Paleoceanography, 21, 1–11, 2006.
Gherardi, J.-M., Labeyrie, L., McManus, J., Francois, R., Skinner, L. C., and Cortijo, E.: Evidence from the Northeastern Atlantic basin for variability in the rate of the meridional overturning circulation through the last deglaciation, Earth Planet. Sci. Lett., 240, 710–723, 2005.
González, C., Dupont, L. M., Behling, H., and Wefer, G.: Neotropical vegetation response to rapid climate changes during the last lacial period: Palynological evidence from the Cariaco Basin, Quaternary Res., 69, 217–230, 2008.
Harrison, S. P. and Prentice, I. C.: Climate and CO_2 controls on global vegetation distribution at the last glacial maximum: analysis based on palaeovegetation data, biome modelling and palaeoclimate simulations, Glob. Change Biol., 9, 983–1004, 2003.
Harrison, S. P., Yu, G., Takahara, H., and Prentice, I. C.: Palaeovegetation – diversity of temperate plants in East Asia, Nature, 413, 129–130, 2001.
Hemming, S. R.: Heinrich events: massive late pleistocene detritus layers of the North Atlantic and their global climate imprint, Rev. Geophys., 42, 1-43, RG1005, doi:10.1029/2003RG000128, 2004.
Henrot, A.-J., François, L., Brewer, S., and Munhoven, G.: Impacts of land surface properties and atmospheric CO_2 on the Last Glacial Maximum climate: a factor separation analysis, Clim. Past, 5, 183–202, doi:10.5194/cp-5-183-2009, 2009.
Hessler, I., Dupont, L. M., Bonnefille, R., Behling, H., González, C., Helmens, K. F., Hooghiemstra, H., Lebamba, J., Ledru, M.-P., Lézine, A.-M., Maley, J., Marret, F., and Vincens, A.: Millennial-scale changes in vegetation records from tropical Africa and South America during the last glacial, Quaternary Sci. Rev., 29, 2882–2899, doi:10.1016/j.quascirev.2009.11.029, 2010.
Hibler, W. D.: A dynamic thermodynamic sea ice model, J. Phys. Oceanogr., 9, 815–846, 1979.
Hughen, K. A., Eglinton, T. I., Xu, L., and Makou, M.: Abrupt tropical vegetation response to rapid climate changes, Science, 304, 955–1959, 2004.
Hunke, E. C. and Dukowicz, J. K.: An elastic-viscous-plastic model for sea ice dynamics, J. Phys. Oceanogr., 27, 1849–1867, 1997.
Jennerjahn, T. C., Ittekkot, V., Arz, H. W., and Behling, H.: Asynchronous terrestrial and marine signals of climate change during Heinrich Events, Science, 306, 2236–2239, 2004.
Kageyama, M., Combourieu Nebout, N., Sepulchre, P., Peyron, O., Krinner, G., Ramstein, G., and Cazet, J.-P.: The Last Glacial Maximum and Heinrich Event 1 in terms of climate and

CPD
7, 1973–2019, 2011

vegetation around the Alboran Sea: a preliminary model-data comparison, Comp. Rend. Geosci., 337, 983–992, 2005.

Kageyama, M., Laîné, A., Abe-Ouchi, A., Braconnot, P., Cortijo, E., Crucifix, M., de Vernal, A., Guiot, J., Hewitt, C. D., Kitoh, A., Marti, O., Ohgaito, R., Otto-Bliesner, B., Peltier, W. R., Rosell-Melé, A., Vettoretti, G., Weber, S. L., and MARGO Project Members.: Last Glacial Maximum temperature over the North Atlantic, Europe and Western Siberia: a comparison between PMIP models, MARGO sea-surface temperatures and pollen-based reconstructions, Quaternary Sci. Rev., 25, 2082–2102, 2006.

Kageyama, M., Mignot, J., Swingedouw, D., Marzin, C., Alkama, R., and Marti, O.: Glacial climate sensitivity to different states of the Atlantic Meridional Overturning Circulation: results from the IPSL model, Clim. Past, 5, 551–570, doi:10.5194/cp-5-551-2009, 2009.

Kageyama, M., Paul, A., Roche, D. M., and Van Meerbeeck, C. J.: Modelling glacial climatic millennial-scale variability related to changes in the Atlantic meridional overturning circulation: a review, Quaternary Sci. Rev., 29, 2931–2956, 2010.

Kalnay, E., Kanamitsu, M., Kistler, R., Collins, W., Deaven, D., Gandin, L., Iredella, M., Saha, S., White, G., Woollen, J., Zhu, Y., Chelliah, M., Ebisuzaki, W., Higgins, W., Janowiak, J., Mo, K. C., Ropelewski, C., Wang, J., Leetmaa, A., Reynolds, R., Jenne, R., and Dennis Joseph.: The NCEP/NCAR 40-Year Reanalysis Project, B. Am. Meteorol. Soc., 77(3), 437–471, 1996.

Kaplan, J. O., Bigelow, N. H., Bartlein, P. J., Christensen, T. R., Cramer, W., Harrison, S. P., Matveyeva, N. V., McGuire, A. D., Murray, D. F., Prentice, I. C., Razzhivin, V. Y., Smith, B., Walker, D. A., Anderson, P. M., Andreev, A. A., Brubaker, L. B., Edwards, M. E., Lozhkin, A. V., and Ritchie, J.: Climate change and Arctic ecosystems II: Modeling, palaeodata-model comparisons, and future projections, J. Geophys. Res., 108, 8171, doi:10.1029/2002JD002559, 2003.

Köhler, P., Joos, F., Gerber, S., and Knutti, R.: Simulated changes in vegetation distribution, land carbon storage, and atmospheric CO_2 in response to a collapse of the North Atlantic thermohaline circulation, Clim. Dynam., 25, 689–708, 2005.

Lamy, F., Kaiser, J., Arz, H. W., Hebbeln, D., Ninnemann, U. S., Timm, O., Timmermann, A., and Toggweiler, J. R.: Modulation of the bipolar seesaw in the Southeast Pacific during Termination 1, Earth Planet. Sci. Lett., 259, 400–413, 2007.

Ledru, M.-P., Ceccantini, G., Gouveia, S. E. M., Lopez-Saez, J. A., Pessenda, L. C. R., and Ribeiro, A. S.: Millenial-scale climatic and vegetation changes in a northern Cerrado (North-

CPD
7, 1973–2019, 2011

east, Brazil) since the Last Glacial Maximum, Quaternary Sci. Rev., 25, 1110–1126, 2006.
Loveland, T. R., Reed, B. C., Brown, J. F., Ohlen, D. O., Zhu, S., Yang, L., and Merchant, J. W.: Developments of a global land cover characteristics database and IGBP DISCover from 1 km AVHRR data, Int. J. Remote Sens., 21, 1303–1330, 2000.
Lumpkin, R. and Speer, K.: Global ocean meridional overturning, J. Phys. Oceanogr., 37, 2250–2262, 2007.
Marchal, O., François, R., Stocker, T. F., and Joos, F.: Ocean thermohaline circulation and sedimentary $^{231}Pa/^{230}Th$ ratio, Paleoceanography, 15, 625–641, 2000.
MARGO Project Members: Constraints on the magnitude and patterns of ocean cooling at the Last Glacial Maximum, Nat. Geosci., 2, 127–132, 2009.
McManus, J. F., Francois, R., Gherardi, J.-M., Keigwin, L. D., and Brown-Leger, S.: Collapse and rapid resumption of Atlantic meridional circulation linked to deglacial climate changes, Nature, 428, 834–837, 2004.
Meissner, K. J., Weaver, A. J., Matthews, H. D., and Cox, P. M.: The role of land surface dynamics in glacial inception: a study with the UVic Earth System model, Clim. Dynam., 21, 515–537, 2003.
Menviel, L., Timmermann, A., Mouchet, A., and Timm, O.: Meridional reorganizations of marine and terrestrial productivity during Heinrich events, Paleoceanography, 23, 2008.
Mulitza, S, Prange, M., Stuut, J.-B., Zabel, M., Dobeneck, T. V., Itambi, A. C., Nizou, J., Schulz, M., and Wefer, G.: Sahel megadroughts triggered by glacial slowdowns of Atlantic meridional overturning, Paleoceanography, 23, 1–11, PA4206, doi:10.1029/2008PA001637, 2008.
Otto-Bliesner, B. L., Brady, E. C., Clauzet, G., Tomas, R., Levis, S., and Kothavala, Z.: Last Glacial Maximum and Holocene Climate in CCSM3, J. Climate, 19, 2526–2544, 2006.
Otto-Bliesner, B. L., Hewitt, C. D., Marchitto, T. M., Brady, E., Abe-Ouchi, A., Crucifix, M., Murakami, S., and Weber, S. L.: Last Glacial Maximum ocean thermohaline circulation: PMIP2 model intercomparisons and data constraints, Geophys. Res. Lett., 34, 1–6, L12706, doi:10.1029/2007GL029475, 2007.
Pacanowski, R. C.: MOM 2 Documentation: Users Guide and Reference Manual, Version 1.0. GFDL Ocean Group Technical Report No. 3, Geophysical Fluid Dynamics Laboratory, Princeton, New Jersey, 1995.
Peltier, W. R.: Ice age paleotopography, Science, 265, 195–201, 1994.
Peterson, L. C., Haug, G. H., Hughen, K. A., and Röhl, U.: Rapid changes in the hydrologic

CPD
7, 1973–2019, 2011

cycle of the tropical Atlantic during the last glacial, Science, 290, 1947–1951, 2000.
Pickett, E., Harrison, S. P., Hope, G., Harle, K., Dodson, J. R., Kershaw, A. P., Prentice, I. C., Backhouse, J., Colhoun, E. A., D'Costa, D., Flenley, J., Grindrod, J., Haberle, S., Hassell, C., Kenyon, C., Macphail, M., Martin, H., Martin, A. H., McKenzie, M., Newsome, J. C., Penny, D., Powell, J., Raine, I., Southern, W., Stevenson, J., Sutra, J.-P., Thomas, I., van der Kaars, S., and Ward, J.: Pollen-based reconstructions of biome distributions for Australia, South East Asia and the Pacific (SEAPAC region) at 0, 6000 and 18 000 ^{14}C yr BP, J. Biogeogr., 31, 1381–1444, 2004.
Prentice, I. C., Cramer, W., Harrison, S. P., Leemans, R., Monserud, R. A., and Solomon, A. M.: A global biome model based on plant physiology and dominance, soil properties and climate, J. Biogeogr., 19, 117–134, 1992.
Prentice, I. C., Jolly, D., and BIOME 6000 Members.: Mid-Holocene and glacial-maximum vegetation geography of the northern continents and Africa, J. Biogeogr., 27, 507–519, 2000.
Prentice, I. C. and Webb III, T.: BIOME 6000: reconstructing global mid-Holocene vegetation patterns from paleoecological records, J. Biogeogr., 25, 997–1005, 1998.
Ray, N. and Adams, J. M.: A GIS-based Vegetation Map of the World at the Last Glacial Maximum (25 000–15 000 BP), Internet Archaeology, 11, available at: http://intarch.ac.uk/journal/issue11/rayadams_toc.html, 2001.
Roche, D. M., Dokken, T. M., Goosse, H., Renssen, H., and Weber, S. L.: Climate of the Last Glacial Maximum: sensitivity studies and model-data comparison with the LOVECLIM coupled model, Clim. Past, 3, 205–224, doi:10.5194/cp-3-205-2007, 2007.
Schmitter, A., Meissner, K. J., Eby, M., and Weaver, A. J.: Forcing of the deep ocean circulation in simulations of the Last Glacial Maximum, Paleoceanography, 17(2), 5:1–5:15, 1015, doi:10.1029/2001PA000633, 2002.
Scholze, M., Knorr, W., and Heimann, M.: Modelling terrestrial vegetation dynamics and carbon cycling for an abrupt climatic change event, Holocene, 13, 327–333, 2003.
Swingedouw, D., Mignot, L. J., Braconnot, P., Mosquet, E., Kageyama, M., and Alkama, R.: Impact of freshwater release in the North Atlantic under different climate conditions in an OAGCM, J. Climate, 22, 6377–6401, 2009.
Vidal, L., Labeyrie, L., Cortijo, E., Arnold, M., Duplessy, J., Michel, E., Becque, S., and van-Weering, T.: Evidence for changes in the North Atlantic DeepWater linked to meltwater surges during the Heinrich events, Earth Planet. Sci. Lett., 146, 13–27, 1997.
Weaver, A. J., Eby, M., Wiebe, E. C., Bitz, C. M., Duffy, P. B., Ewen, T. L., Fanning, A. F.,

CPD
7, 1973–2019, 2011

Holland, M. M., MacFadyen, A., Matthews, H. D., Meissner, K. J., Saenko, O., Schmittner, A., Wang, H., and Yoshimori, M.: The UVic Earth System Climate Model: model description, climatology, and applications to past, present and future climates, Atmos.-Ocean, 39, 361–428, 2001.

Weaver, A. J., Saenko, O. A., Clark, P. U., and Mitrovica, J. X.: Meltwater pulse 1A from Antarctica as a trigger of the Bølling-Allerød warm interval, Science, 299, 1709–1713, 2003.

Weber, S. L. and Drijfhout, S. S.: Stability of the Atlantic meridional overturning circulation in the Last Glacial maximum climate, Geophys, Res. Lett., 34, 1-5, L22706, doi:10.1029/2007GL031437, 2007.

Yokoyama, Y., De Deckker, P., Lambeck, K., Johnston, P., and Fifield, L. K.: Sea-level at the last glacial maximum: evidence from Northwestern Australia to constrain ice volumes for oxygen isotope stage 2, Palaeogeogr. Palaeocl., 165, 281–297, 2001.

Yu, E. F., Francois, R., and Bacon, M. P.: Similar rates of modern and last-glacial ocean thermohaline circulation inferred from radiochemical data, Nature, 379, 689–694, 1996.

CPD

7, 1973–2019, 2011

Table 1. Boundary conditions (including atmospheric CO_2 in atmosphere, amount and location for freshwater perturbation) and simulation design for all simulations analysed in the present paper.

Simulation	Orbital parameter	CO_2 concentration	Freshwater anomaly amount (Sv)	Location	Years simulation
Equilibrium					
PI_CNTRL	Pre-industrial	280			2000
LGM	21 ka BP	200			2000
Heinrich event					
HE1_IGL	Pre-industrial	280	0.1	A	500
HE1_GL	21 ka BP	200	0.1	A	500

CPD
7, 1973–2019, 2011

Table 2. Distribution of dominant PFTs which is based on the percentage of PFT coverage.

Dominant PFTs or PFTs mixture	PFT coverage
	BL, NL, SH, C_3, C_4 over 50 %
Broadleaved trees (BL)	BL ≥ 50 %
Needleleaved trees (NL)	NL ≥ 50 %
Shrubs (SH)	SH ≥ 50 %
C_3 grass (C_3)	C_3 ≥ 50 %
C_4 grass (C_4)	C_4 ≥ 50 %
	BL, NL, SH, C_3, C_4 less than 50 %
Mixed trees	BL + NL ≥ 50 %
Mixed vegetation (without trees)	SH + C_3 + C_4 ≥ 50 %
Open vegetation	20 % ≤ BL + NL + SH + C_3 + C_4 ≥ 50 %
Barren soil	BL + NL + SH + C_3 + C_4 < 20 %

The dominant PFT in each grid cell is evaluated based on the percentage of PFT coverage. If the percentage of PFT coverage is over 50 %, the PFT potential is set equal to the dominant PFT (broadleaved trees, needleleaved trees, shrubs, C_3 grass, or C_4 grass). If it is less than 50 %, the grid cell is designated as mixed trees if it is dominated by tree PFTs, mixed vegetation if non-trees PFTs are dominant, open vegetation if all PFTs are between 20 % and 50 %, and desert if all PFTs together is less than 20 % (Crucifix, 2005).

CPD
7, 1973–2019, 2011

Table 3. The combination of environmental constrains and potential PFTs are used to compute the biome distribution from UVic ESCM results.

Biome	Dominant PFTs or PFTs mixture	Environmental constrain				
		Tc min	GDD5 min	GDD0 min	Tw min	Tw max
Tropical forest	BL trees	15.5				
Warm-temperate forest	BL trees or mixed trees	5				
Temperate forest	BL trees or NL trees or mixed trees	−2				
Boreal forest	BL trees or NL trees or mixed trees	−32.5				
Savanna and dry woodland	Grass or mixed vegetation or open vegetation	17				
Grassland and dry shrubland	Grass or mixed vegetation or open vegetation		500		10	
Desert	Barren soil				22	
Dry tundra	SH or mixed vegetation					15
Tundra	SH or mixed vegetation			800		15

The land temperatures from the UVic ESCM are used to calculate the temperature of the coldest month (Tc), growing degree-days relative to 0 °C and 5 °C (GDD5 and GDD0), and temperature of the warmest month (Tw) following BIOME4 (Kaplan et al., 2003). The assignment of a particular biome to a grid cell is based on the BIOME 6000 project version 4.2 after Prentice et al. (1992), Harrison and Prentice (2003), and Roche et al. (2007).

CPD
7, 1973–2019, 2011

Table 4. Comparison of tropical mega-biomes during HE1 period between pollen reconstructions (compiled by Hessler et al., 2010) and model results (computed from HE1_GL using UVic ESCM). The site locations for pollen reconstruction are in Equatorial Africa and South America from terrestrial and marine sites (shown in Fig. 1). Blue plus sign denotes if data and model results are similar and the red plus sign denotes if data and model results are different.

No.	Latitude and Longitude	Site location name	Potential biome distribution		Comparison between data and model
			Pollen data	Model result	
	Equatorial Africa				
	Terrestrial site				
1.	3.47° S–29.57° E	Kashiru Bog, Burundi	– Grassland and dry shurbland – Savannah and xerophytic scrubland	Tropical forest	+
2.	8.50° S–30.85° E	Lake Tanganyika	– Warm temperate mixed forest – Savannah and xerophytic scrubland	– Boreal forest – Savannah and dry-woodland	+
3.	9.33° S–33.75° E	Lake Masoko, Tanzania	– Warm temperate mixed forest – Savannah and xerophytic scrubland	Savannah and dry-woodland	+
4.	11.29° S–34.44° E	Lake Malawi	– Savannah and xerophytic scrubland – Tropical forest	Savannah and dry-woodland	+
6.	4.51° N–9.40° E	Barombi Mbo, Cameroon	– Savannah and xerophytic scrubland – Tropical forest	Tropical forest	+
	Marine site				
5.	4.40° N–4.18° W	off Ivory Coast, KS 84-063	– Tropical forest – Warm temperate mixed forest	Tropical forest	+
7.	11.92° S–13.40° E	ODP 1078C – Angola	– Warm temperate mixed forest – Temperate-montane forest	– Tropical forest – Temperate forest	+

CPD
7, 1973–2019, 2011

Table 4. Continued.

No.	Latitude and Longitude	Site location name	Potential biome distribution Pollen data	Potential biome distribution Model result	Comparison between data and model
8.	17.15° S–11.02° E	GeoB 1023 – Cunene River Mouth	– Savannah and xerophytic scrubland – Grassland and dry shurbland	Grassland and shrubland	+
	South America				
	Terrestrial site				
11.	2.97° S–43.42° W	Lake Caçó – NE Brazil	– Warm temperate mixed forest – Tropical forest	Tropical forest	+
12.	23.87° S–46.71° W	Colônia, Brazil	– Savannah and xerophytic scrubland – Grassland and dry shurbland	– Temperate forest – Grassland and dry shrubland	+
13.	17.83° S–64.72° W	Siberia, Bolivia	– Temperate-montane forest – Grassland and dry shurbland	Temperate forest	+
14.	4.92° N–74.03° W	La Laguna, Bogotà, Colombia	– Savannah and xerophytic scrubland – Grassland and dry shurbland	Tropical forest	+
15.	5.45° N–73.46° W	Fúquene, Colombia	– Savannah and xerophytic scrubland – Temperate-montane forest	Tropical forest	+
	Marine site				
9.	3.67° S–37.72° W	GeoB 3104 – off NE Brazil	– Temperate-montane forest – Warm temperate mixed forest	Tropical forest	+
10.	4.15° S–36.21° W	GeoB 3910-2 – off NE Brazil	– Savannah and xerophytic scrubland – Warm temperate mixed forest	Tropical forest	+

CPD
7, 1973–2019, 2011

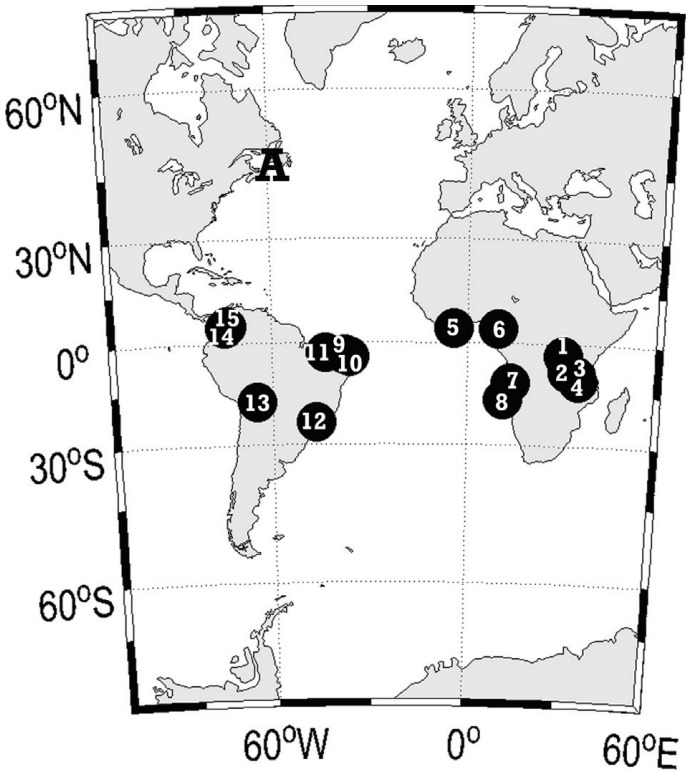

Fig. 1. Freshwater discharge location for our Heinrich event 1 climate-like simulations (St. Lawrence River, location A) and paleovegetation proxy locations (fifteen black circles, number refer to the sites listed in Table 1) covering the Heinrich event 1 period from Hessler et al. (2010) in Tropical Africa and South America.

CPD
7, 1973–2019, 2011

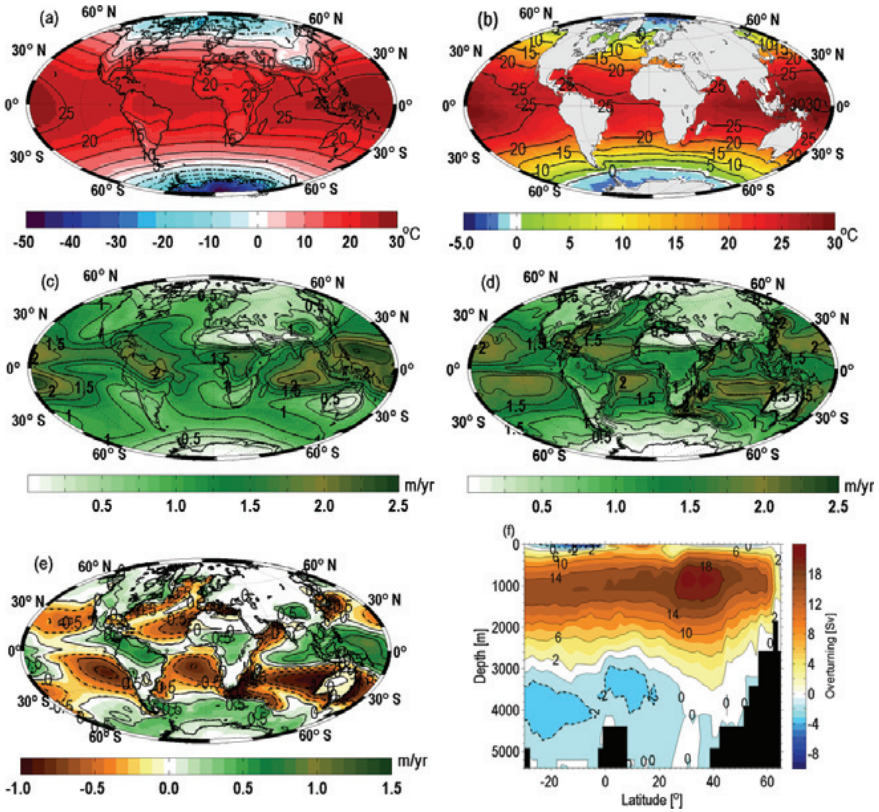

Fig. 2. Annual-mean of **(a)** surface air temperature (SAT), **(b)** sea surface temperature (SST), **(c)** precipitation, **(d)** evaporation, **(e)** precipitation minus evaporation (P – E), and **(f)** zonally integrated meridional overturning streamfunction in the North Atlantic for the pre-industrial simulation (PI_CNTRL). Contour intervals in SAT and SST are 5 °C. Contour intervals of the streamfuction of AMOC formation is 4 Sv (1 Sv = 10^6 m^3 s^{-1}). Solid line contours indicate a clockwise circulation while dotted lines denote a counterclock-wise circulation.

CPD
7, 1973–2019, 2011

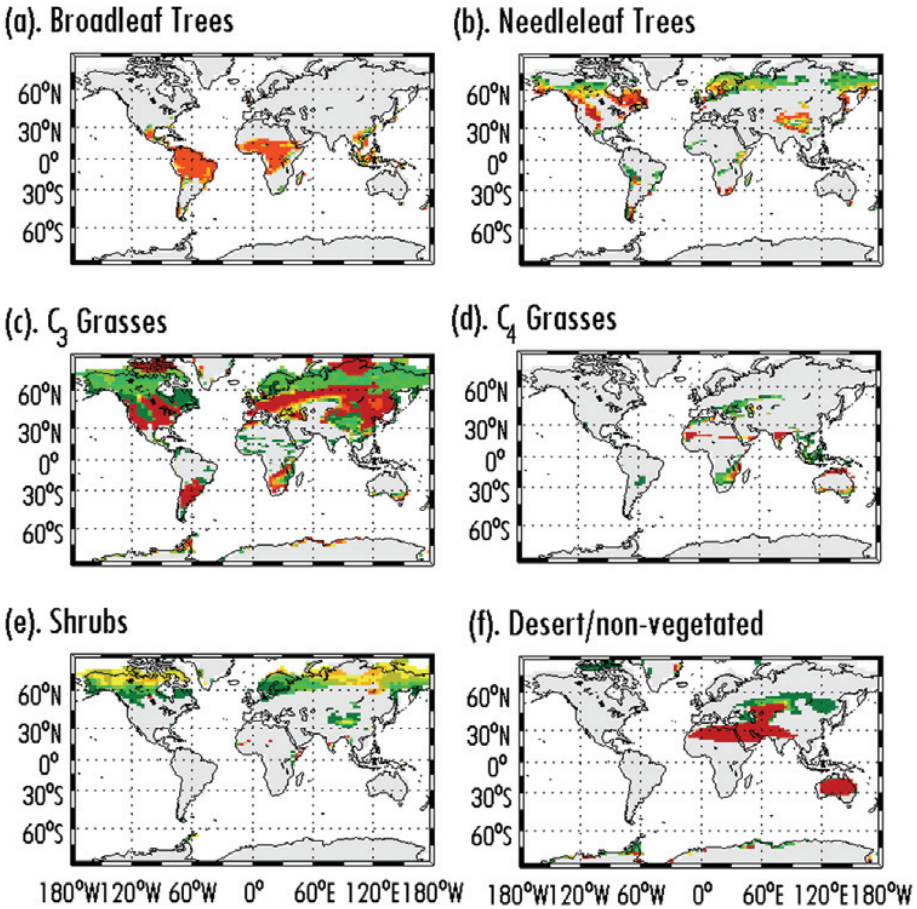

Fig. 3. Annual-mean of plant functional type (PFT) covers for; **(a)** broadleaf trees, **(b)** needleleaf trees, **(c)** C_3 grass, **(d)** C_4 grass, **(e)** shrubs, and bare soil coverage **(f)** desert/not vegetated for the PI_CNTRL simulation.

CPD
7, 1973–2019, 2011

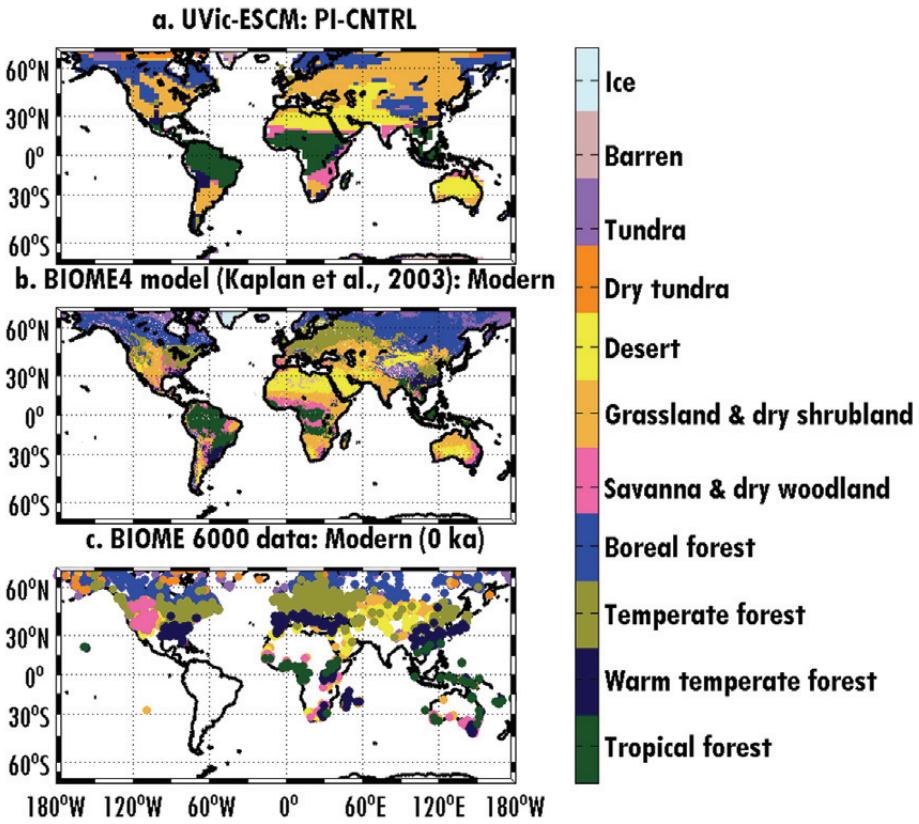

Fig. 4. Mega-biome distribution for **(a)** PI_CNTRL biomes simulated in UVic ESCM, **(b)** modern biomes by the BIOME 4 (Kaplan et al., 2003), and **(c)** mapping of modern pollen samples by BIOME 6000 (Prentice and Webb, 1998). The UVic ESCM biomes compute as a combination of environmental constrains and potential PFTs, and the mega-biomes distribution is grouped Harrison and Prentice (2003).

CPD
7, 1973–2019, 2011

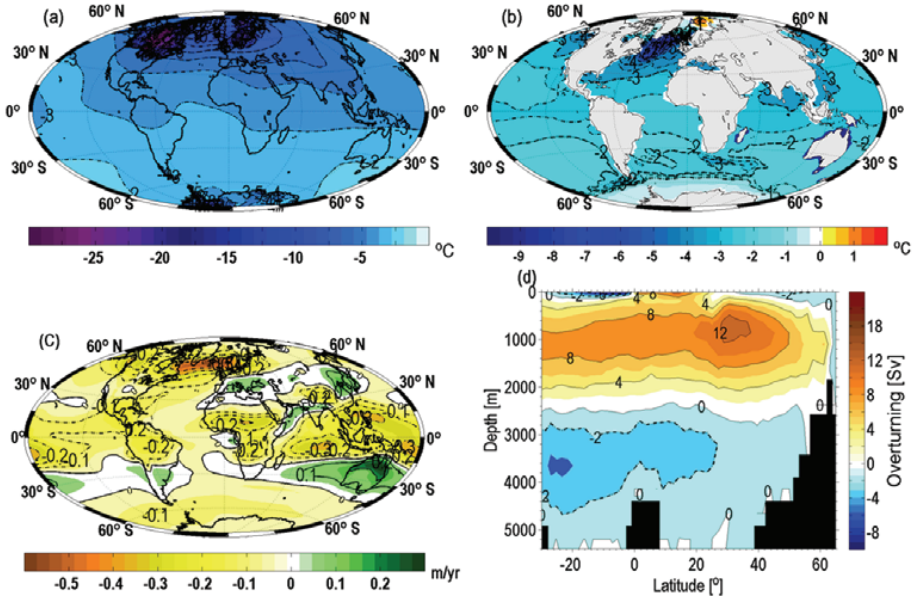

Fig. 5. Annual-mean anomaly showing differences between the LGM and the PI_CNTRL simulations for: **(a)** surface air temperature (SAT), **(b)** sea surface temperature (SST), and **(c)** precipitation. **(d)** denotes the zonally integrated meridional overturning streamfunction (Sv) in the North Atlantic for the LGM simulation with a fixed volume contour interval of 4 Sv similar as Fig. 2f. Contour intervals for SAT and SST are 1 °C.

CPD
7, 1973–2019, 2011

Tropical climate and vegetation changes during Heinrich Event 1

D. Handiani et al.

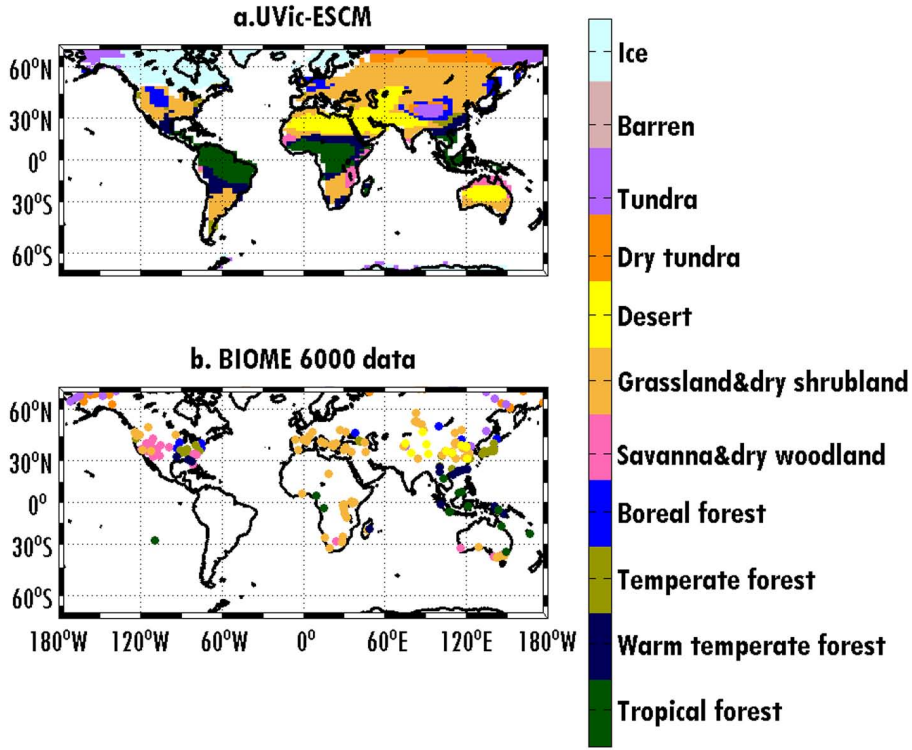

Fig. 6. Mega-biome distribution for the last glacial maximum (LGM, 21 ka BP): **(a)** LGM biomes simulated by the UVic ESCM, **(b)** paleovegetation mapping by BIOME 6000 (Prentice and Webb, 1998).

CPD
7, 1973–2019, 2011

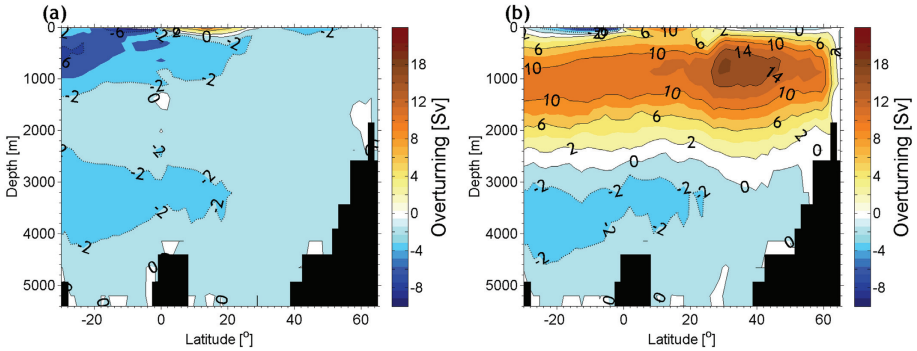

Fig. 7. Zonally integrated meridional overturning streamfunction (Sv) in the North Atlantic after 500 yr of **(a)** HE1_GL and **(b)** HE1_IGL simulations. Contour interval is a fixed volume of 4 Sv ($1\,\mathrm{Sv} = 10^6\,\mathrm{m}^3\,\mathrm{s}^{-1}$). Solid line contours indicate a clockwise circulation and dotted line contours denote a counterclockwise circulation.

CPD
7, 1973–2019, 2011

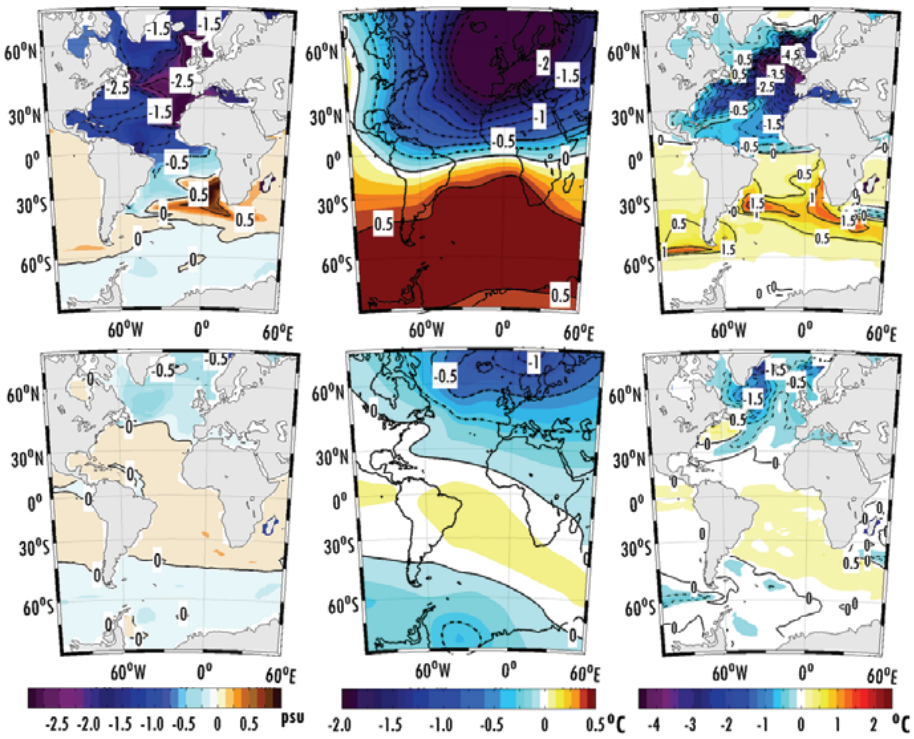

Fig. 8. Annual-mean anomaly showing differences between the HE1_GL and the LGM simulations (top) and the HE1_IGL and the PI_CNTRL simulations (bottom) for sea surface salinity (SSS, left), surface air temperature (SAT, middle), and sea surface temperature (SST, right).

CPD
7, 1973–2019, 2011

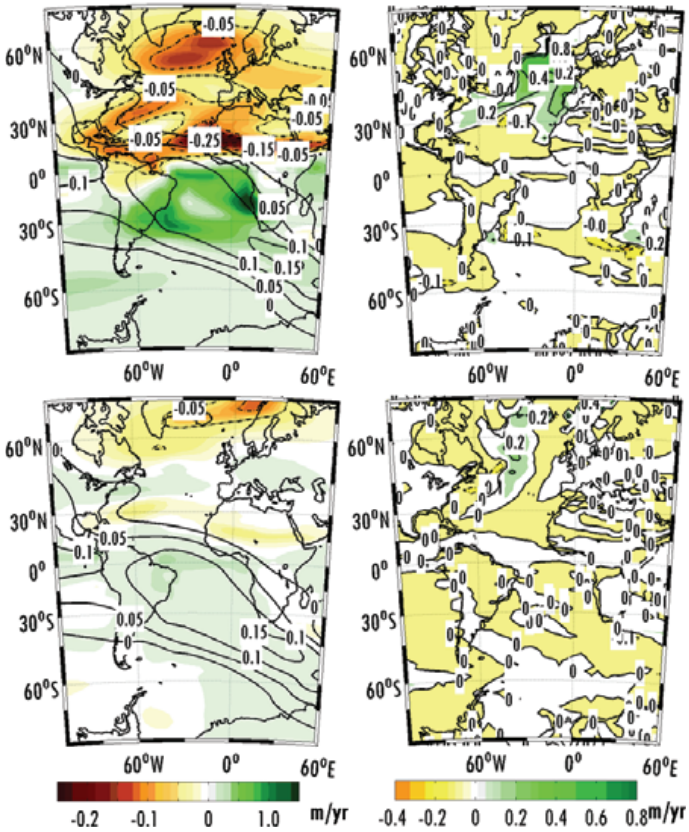

Fig. 9. Annual-mean anomaly showing differences between the HE1_GL and the LGM simulations (top) and the HE1_IGL and the PI_CNTRL simulations (bottom) for precipitation (left), and net flux freshwater (precipitation – evaporation – runoff, P – E – R, right).

CPD
7, 1973–2019, 2011

Tropical climate and vegetation changes during Heinrich Event 1

D. Handiani et al.

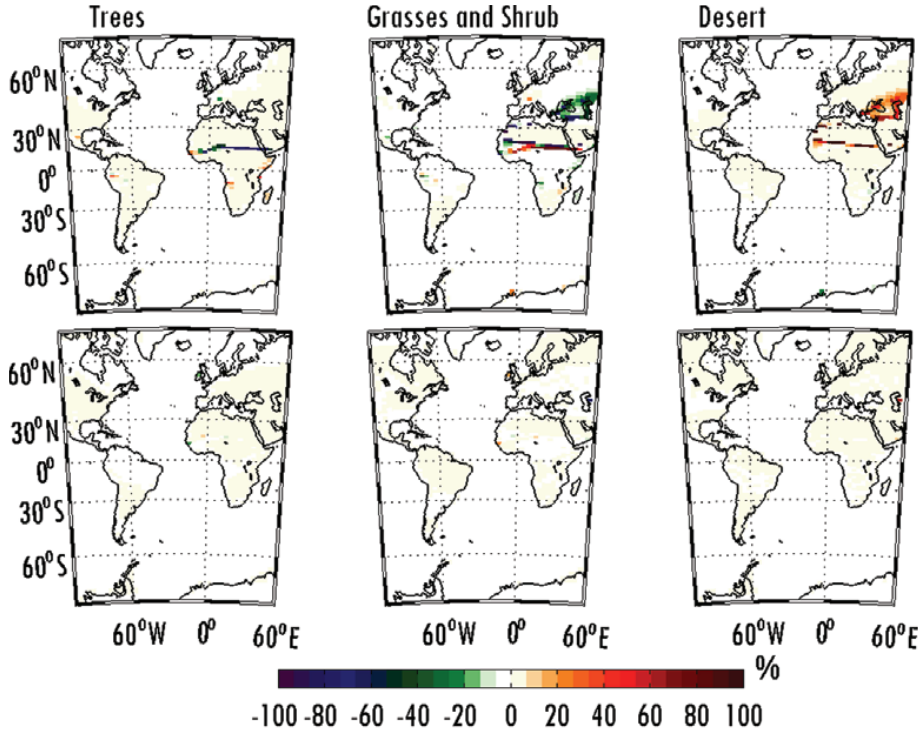

Fig. 10. Annual-mean PFT differences in percent coverage between HE1_GL and LGM (top) and HE_IGL and PI_CNTRL (below) for trees (left), grasses and shrubs (middle), and desert, non-vegetated coverage (right).

CPD
7, 1973–2019, 2011

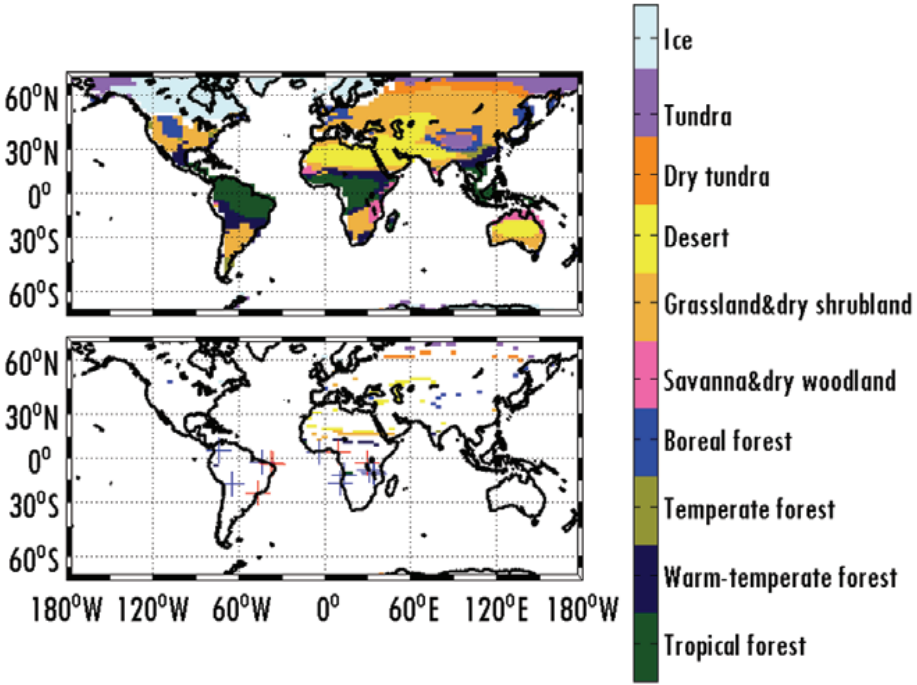

Fig. 11. Mega-biome distribution computed from UVic ESCM results; (top) HE1_GL simulation and (bottom) anomaly between HE_GL and LGM simulations. The anomaly map shows the HE1_GL biome only in those grid cells that differ from the LGM simulation. Blue crosses indicate locations where biomes are similar in the model and the data reconstruction (Hessler et al., 2010); red crosses denote where modeled and reconstructed biomes differ.

CPD
7, 1973–2019, 2011